

# Broadband Spintronic Detection of the Absolute Field Strength of Terahertz Electromagnetic Pulses

A.L. Chekhov<sup>1,\*</sup>, Y. Behovits,<sup>1</sup> U. Martens,<sup>2</sup> B.R. Serrano,<sup>1</sup>  
M. Wolf,<sup>3</sup> T.S. Seifert,<sup>1</sup> M. Münzenberg,<sup>2</sup> and T. Kampfrath<sup>1,3</sup>

<sup>1</sup>Department of Physics, Freie Universität Berlin, Arnimallee 14, 14195 Berlin, Germany

<sup>2</sup>Institut für Physik, Universität Greifswald, Felix-Hausdorff-Straße 6, 17489 Greifswald, Germany

<sup>3</sup>Fritz Haber Institute of the Max Planck Society, Faradayweg 4-6, 14195 Berlin, Germany



(Received 15 June 2023; revised 10 August 2023; accepted 17 August 2023; published 18 September 2023)

We demonstrate the detection of broadband intense terahertz electromagnetic pulses by Zeeman-torque sampling (ZTS). Our approach is based on magneto-optic probing of the Zeeman torque that the terahertz magnetic field exerts on the magnetization of a ferromagnet. Using an 8-nm-thick iron film as a sensor, we detect pulses from a silicon-based spintronic terahertz emitter with a bandwidth of 0.1–11 THz and a peak field of  $>0.1$  MV/cm. A simple static magneto-optic calibration measurement provides access to absolute transient terahertz field strengths. We show the relevant added value of ZTS compared to electro-optic sampling (EOS): an echo-free transfer function with simple frequency dependence, linearity even at high terahertz-field amplitudes, the straightforward calibration of EOS response functions, and modulation of the polarization-sensitive direction by an external ac magnetic field. Consequently, ZTS has interesting applications even beyond the accurate characterization of broadband high-field terahertz pulses for nonlinear terahertz spectroscopy.

DOI: 10.1103/PhysRevApplied.20.034037

## I. INTRODUCTION

Recently developed high-field table-top terahertz (THz) sources [1–6] allow one to resonantly drive numerous low-energy excitations in all phases of matter into previously inaccessible regimes [7–9]. Examples include the nonlinear excitation of magnons [10], nonlinear magnon dynamics [11–13], magnon-phonon coupling [14], the nonlinear THz Kerr effect in liquids [15], and the phononic switching [16,17] or generation [18] of magnetic order. For such experiments, it is essential to accurately determine the time-dependent electric field  $\mathbf{E}$  and magnetic field  $\mathbf{B}$  of the driving THz pulse at a given position.

The state-of-the-art method for THz-pulse detection is electro-optic sampling [EOS, Fig. 1(a)]. It is based on the linear electro-optic (EO) effect in the sensing material, i.e., an anisotropic variation of the material's refractive index along certain eigendirections (linear birefringence), which is proportional to the applied transient electric field. EOS requires crystals with broken inversion symmetry, such as

ZnTe, GaP, or GaAs. The THz-field-induced transient birefringence  $S(t)$  is typically measured by an optical probe pulse as a function of the delay  $t$  between THz and optical probe pulses [Fig. 1(a)].

Determination of  $\mathbf{E}(t)$  from  $S(t)$  requires accurate knowledge of the EOS transfer function, which is strongly frequency dependent in the vicinity of phonon resonances, typically in the range of 5–15 THz [19]. As a result, extraction of the transient THz electric field  $\mathbf{E}(t)$  in particular, absolute field strengths, from the measured  $S(t)$  is nontrivial. This issue is most severe when the THz pulses cover large frequency intervals of, e.g., 1–10 THz and beyond, like those obtained by optical rectification in organic crystals [20] or from photocurrents in spintronic THz emitters [6,21].

An interesting alternative route to THz-pulse detection is offered by the THz magnetic field  $\mathbf{B}(t)$ . In ferro- or ferrimagnets,  $\mathbf{B}$  straightforwardly couples to the magnetization  $\mathbf{M}$  of the material by Zeeman torque (ZT) and, thus, drives ultrafast magnetization dynamics [Fig. 1(b)] [22–28]. So far, ZT has been used to manipulate  $\mathbf{M}$  with bandwidths up to 5 THz [25].

Here, we show that the magnetization dynamics in a ferro- or ferrimagnet driven by the ZT of the magnetic component of THz pulses can be used to measure intense transient THz electric fields of  $>0.1$  MV/cm over the entire range of 0.1–11 THz. We optimize the THz ZT-detector

\* a.chekhov@fu-berlin.de

Published by the American Physical Society under the terms of the [Creative Commons Attribution 4.0 International license](#). Further distribution of this work must maintain attribution to the author(s) and the published article's title, journal citation, and DOI. Open access publication funded by the Max Planck Society.

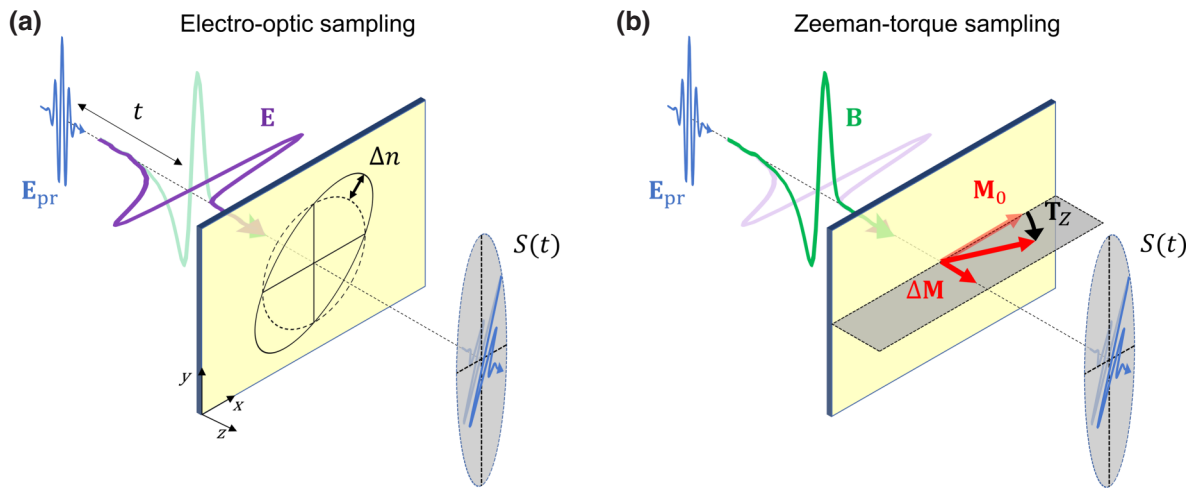


FIG. 1. Schematics of THz-electromagnetic-field detection by (a) EOS and (b) ZTS. In EOS, the THz electric field  $\mathbf{E}$  induces an anisotropic change  $\Delta n$  in the refractive index and, thus, a linear optical birefringence of the detection material (dashed circle and solid ellipse). In contrast, in ZTS, the THz magnetic field  $\mathbf{B}$  exerts Zeeman torque  $\mathbf{T}_Z$  on the magnetization  $\mathbf{M}$  of the magnetic sample and, thus, induces a transient circular optical birefringence (Faraday effect).

composition to achieve the best performance in terms of signal-to-noise ratio and bandwidth. The response function of ZT sampling (ZTS) is found to have a simple frequency dependence, and its absolute magnitude can be calibrated by a static magnetic field. As a first application, we use our detection method to determine the response function of commercial EOS crystals. Second, we demonstrate modulation of the Zeeman-detector response at kilohertz rates with an external magnetic field, thereby enabling demodulation schemes of THz waves.

## II. ZT DETECTION

In our ZTS approach [Fig. 1(b)], the THz pulse to be measured and an optical probe pulse are normally incident on a magnetic thin film, the static magnetization  $\mathbf{M}_0$  of which lies in the film plane. The magnetic field  $\mathbf{B}(t)$  of the THz pulse exerts a torque proportional to  $\mathbf{M} \times \mathbf{B}$  and, thus, deflects the dynamic magnetization  $\mathbf{M}$  out of the plane. For sufficiently small fields, the magnetization change  $\Delta\mathbf{M} = \mathbf{M} - \mathbf{M}_0$  is given by

$$\Delta\mathbf{M}(t) = \gamma\mathbf{M}_0 \times \int_{-\infty}^t dt' \mathbf{B}(t'), \quad (1)$$

where  $\gamma$  is the electron gyromagnetic ratio. The optical probe pulse detects the out-of-plane component of  $\Delta\mathbf{M}$ , averaged over the probed volume, by the Faraday effect, i.e., the circular birefringence induced by  $\Delta\mathbf{M}$ . As shown in Appendix A, the birefringence signal at THz frequency  $\omega/2\pi$  is given by

$$\tilde{S}(\omega) = \tilde{H}(\omega)\mathbf{v} \cdot \tilde{\mathbf{E}}_{\text{inc}}(\omega). \quad (2)$$

It is proportional to the projection of the incident THz field  $\tilde{\mathbf{E}}_{\text{inc}}(\omega)$  on the unit-vector direction  $\mathbf{v} = \mathbf{M}_0/|\mathbf{M}_0|$  of the static magnetization. The transfer function

$$\tilde{H}(\omega) = C_E(\omega)C_{\text{pr}} = \frac{b}{i\omega} \quad (3)$$

has two contributions. First, the coefficient  $C_E(\omega) \propto 1/i\omega$  [Eq. (A9)] quantifies the coupling of the incident THz electromagnetic field into the thin film and the coupling strength of  $\mathbf{B}$  to  $\mathbf{M}$ , where the straightforward  $1/i\omega$  frequency dependence arises from the time integration of  $\mathbf{B}$  and, thus,  $\mathbf{E}$  [see Eq. (1)]. Second, the coefficient  $C_{\text{pr}}$  is independent of  $\omega$  [Eq. (A9)] and describes the probe coupling to  $\Delta\mathbf{M}$  and coupling out of the film. All frequency-independent factors of  $C_E(\omega)C_{\text{pr}}$  are summarized by the coefficient  $b$ .

As detailed in Appendix A, Eq. (3) is an approximation that is valid for metallic ZT detectors. Interestingly, in this approximation, the ZT signal of Eq. (2) is in the time domain given by the integral

$$S(t) = -b\mathbf{v} \cdot \int_{-\infty}^t dt' \mathbf{E}_{\text{inc}}(t') \quad (4)$$

and, thus, the vector potential of the incident THz pulse in the radiation gauge, similar to signals obtained by attosecond sampling of light fields [29].

We emphasize that the scaling factor  $b$  of the transfer function  $\tilde{H}(\omega)$  [Eq. (3)] can be determined by a single straightforward static calibration measurement, thereby providing access to the *absolute* strength of the incident THz electric field (see Sec. III C and Appendix B).

### III. EXPERIMENTAL DETAILS

#### A. THz setup

To test the capabilities of ZTS [Fig. 1(b)], we use pump pulses (center wavelength 800 nm, pulse energy 5 mJ, pulse duration 35 fs if bandwidth limited, repetition rate 1 kHz) from an amplified Ti:sapphire laser system to generate intense broadband THz pulses (spectrum 0.1–11 THz, peak field 1.7 MV/cm) in a Si-based spintronic THz emitter (Si-STE, TeraSpinTec GmbH) [6]. As detailed in Fig. S1 [30], the THz focal field is sampled with probe pulses (800 nm, 0.3 nJ, 30 fs, 80 MHz) in the ZT detector. They are derived from the Ti:sapphire oscillator seeding the amplified laser and exhibit excellent stability allowing probing at the shot-noise limit [31].

For referencing, we use EOS in a freestanding GaP(110) crystal (Swiss THz), the thickness of only 50  $\mu\text{m}$  of which facilitates a wide detection window of 0–7 THz and beyond [19]. The EOS response function is analogous to Eq. (2). The transfer function  $\tilde{H}(\omega)$  and the unit-length vector  $\mathbf{v}$  are just replaced by expressions that are determined by the refractive index and quadratic optic response tensor of GaP, as well as the GaP thickness, azimuthal orientation, the probe pulse's electric field, and its linear polarization state [6,32,33].

#### B. ZTS detectors

Because  $C_{\text{pr}}$  is proportional to the thickness  $d$  and the magneto-optic Voigt parameter  $Q \propto |\mathbf{M}_0|$  of the ZT film, the ZTS response is enhanced for films with large  $Q$  and optimum thickness. The latter also depends on the magnitude of the probe transmission. Consequently, we choose the metallic ferromagnet Fe and the insulating ferrimagnetic bismuth-substituted iron garnet  $\text{Bi}_3\text{Fe}_5\text{O}_{12}$  (BiIG).

Fe features the largest Voigt parameter  $|Q| \sim 10^{-2}$  among 3d ferromagnets around the 800-nm probe wavelength [34], but, at the same time, strongly attenuates the probe beam [35]. We, therefore, choose an optimum thickness  $d$  of 8 nm. In contrast, BiIG has a 1 order of magnitude smaller  $|Q| \sim 10^{-3}$ , but 3 orders of magnitude smaller absorption coefficient and lower reflection losses than Fe [36]. At the same time, phonon resonances in the garnet can distort and attenuate the THz pulse [37]. To minimize this effect, we choose a thickness of 4.5  $\mu\text{m}$ .

The Fe(8 nm) film is obtained by electron-beam evaporation under ultrahigh-vacuum conditions onto a glass substrate. The BiIG(4.5  $\mu\text{m}$ ) film (INNOVENT e.V.) with in-plane magnetic anisotropy is grown on a gallium gadolinium garnet substrate by liquid-phase epitaxy. The magnetization  $\mathbf{M}_0$  is set by a Halbach array of permanent magnets and can be reversed by 180° azimuthal rotation [6].

#### C. Calibration

To calibrate our ZT detector, the most straightforward approach would be to completely pull the static magnetization of the ferromagnet out of the plane and measure the resulting Faraday rotation and ellipticity of the probe beam. For our in-plane-magnetized Fe(8 nm) film, this procedure requires static magnetic fields of >2 T, which are not easily available.

Therefore, we apply a saturating in-plane magnetic field of 30 mT along the  $x$  axis [Fig. 1(b)] and measure the magneto-optic response for an  $s$ -polarized probe beam in reflection geometry with an angle of incidence of 52°, i.e., the so-called longitudinal magneto-optic Kerr effect (LMOKE). As detailed in Appendix B and Table S1 [30], this information, along with the optical and THz refractive indices (or conductivities) of Fe and glass, is sufficient to determine the complex-valued scaling factor  $b$  of the transfer function in Eq. (3).

#### D. Signal contributions

In the experiment, the intense THz pulses can induce nonlinear contributions in the THz fields [24,38]. To discriminate quadratic contributions, we measure pump-probe signals  $S_{\pm\mathbf{E},\pm\mathbf{M}_0}$  for opposite polarities of the THz field ( $\pm\mathbf{E}$ ) by reversing the Si STE magnetization direction. Furthermore, to separate odd (linear) effects in the ZT-detector magnetization  $\mathbf{M}_0$ , we alternate the latter ( $\pm\mathbf{M}_0$ ) by means of an ac electromagnet at a frequency of 500 Hz, i.e., half the repetition rate of the THz pulses. The extracted signals  $S = S(t)$ , which are linear in terms of both the driving THz field  $\mathbf{E}$  and the ZT magnetization  $\mathbf{M}_0$  are calculated according to

$$S = \frac{S_{+\mathbf{E},+\mathbf{M}_0} - S_{-\mathbf{E},+\mathbf{M}_0} - S_{+\mathbf{E},-\mathbf{M}_0} + S_{-\mathbf{E},-\mathbf{M}_0}}{4}, \quad (5)$$

as illustrated in Fig. S2 [30].

### IV. ZTS RESULTS

#### A. ZTS raw data

Figure 2(a) shows signal waveforms  $S(t)$  obtained with the various ZT and EO detectors under identical THz-pulse excitation. While the EO signal from GaP and the ZT signal from Fe correspond to probe-ellipticity variation (see Fig. S3 [30]), the ZT signal in BiIG is measured as probe-polarization rotation. A Fourier transformation yields the corresponding signal-amplitude spectra, as shown in Fig. 2(b). For the Fe sample, we confirm that the measured signal  $S(t)$ , which is odd in  $\mathbf{E}$ , grows linearly with  $\mathbf{E}$ . Quadratic contributions to  $\mathbf{E}$  are minor, in particular, ultrafast quenching of the in-plane magnetization,

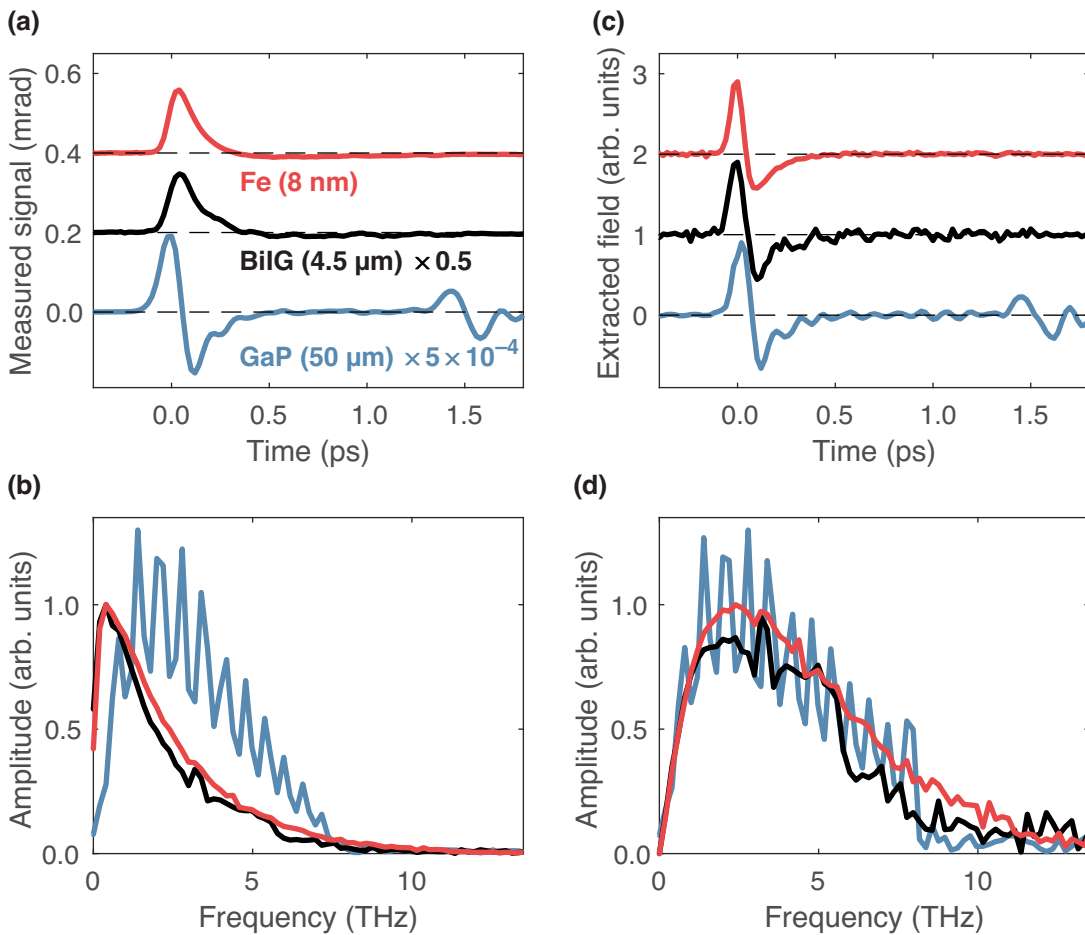


FIG. 2. ZTS and EOS data. (a) Birefringence signals induced by the THz pump pulse obtained via ZTS in Fe(8 nm) (red solid line) and BiIG(4.5  $\mu\text{m}$ ) (black) and, for reference, by EOS in GaP(50  $\mu\text{m}$ ) (blue). (b) Fourier amplitude spectra of the waveforms of panel (a). (c) Transient THz electric fields, obtained by taking the time derivative of the ZTS signals (Fe and BiIG detectors) and by using the calculated EOS transfer function (reference GaP detector). Signals are normalized to their peak value. (d) Fourier amplitude spectra of the waveforms of panel (c).

which is not sensed by the Faraday effect of the normally incident probe pulses (see Fig. S2 [30]).

The EO signal from the GaP(50  $\mu\text{m}$ ) reference detector exhibits a main pulse centered at time  $t = 0$  ps, but also a sizeable echo at  $t = 1.5$  ps [Fig. 2(b)], which results in spectral oscillation with a period of  $1/1.5$  ps = 0.7 THz [Fig. 2(b)]. The echo arises from reflection of the THz pulse at the GaP-air and air-GaP interfaces and limits the time window and, thus, frequency resolution of EOS.

Note that the ZT signals are substantially different from the EO reference signal. First, no echo is found in the covered time window. Second, the ZT signals are reminiscent of the time-integrated EO signal [Fig. 2(a)], as expected from Eq. (1). Interestingly, the ZT signal from Fe is only a factor of 2 smaller than from BiIG but has a somewhat smoother time [Fig. 2(a)] and frequency dependence [Fig. 2(b)].

## B. From signals to incident fields

To extract the THz-field transients from the measured EO and ZT signals of Fig. 2(a), we employ Eq. (2). For EOS,  $\tilde{H}(\omega)$  is obtained from previous work [21,22], while, for ZTS, we need only to take the time derivative  $\partial_t S(t)$  of the measured signal, according to Eq. (3). The resulting normalized THz-electric-field transients and their amplitude spectra are shown in Figs. 2(c) and 2(d), respectively.

All time-domain waveforms [Fig. 2(c)] exhibit a very similar shape, indicating a reliable extraction procedure. For GaP, the extracted THz field still features the echo at  $t = 1.5$  ps in the time domain [Fig. 2(c)] and fringes in the frequency domain [Fig. 2(d)], analogous to the EO signals [Figs. 2(a) and 2(b)]. The reason for this behavior is that the modeled EOS transfer function [21,22] does not take the multiple reflections of the THz pulse inside the GaP crystal into account and, thus, does not correct for them.

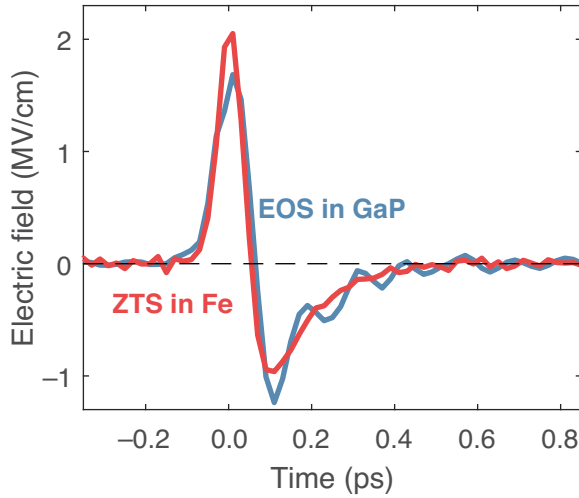


FIG. 3. Absolute THz-field extraction. Back-to-back comparison of the transient incident THz electric field obtained from ZTS and EOS signals of Fe(8 nm) (red curve) and GaP(50  $\mu\text{m}$ ) (blue curve) shown in Fig. 2.

As expected from the ZT signals [Fig. 2(a)], the field trace obtained with Fe(8 nm) is significantly smoother than the trace obtained with BiIG(4.5  $\mu\text{m}$ ). We ascribe this behavior to two effects: (i) a substantial variation of the BiIG refractive index  $n(\omega)$  in the considered frequency interval of 0–12 THz due to the large number of infrared-active optical phonon modes [37], and (ii) long-wavelength quasiantiferromagnetic magnons [27] that may alter the simple  $1/\omega$  scaling of  $C_E$  in Eq. (3). Points (i) and (ii) could, in principle, be accounted for by an appropriate frequency dependence of  $C_E$ .

We note that the refractive index of Fe exhibits dispersion, too. However, as shown in Appendix A and Fig. S6 [30], the resulting frequency dependence of  $C_E(\omega)$  in Eq. (3) can still be well approximated by  $1/\omega$ . To enable ZT detection of broadband THz pulses with a smooth frequency response, we, thus, focus on Fe in the remainder of this work.

### C. Extracting the absolute THz field

As detailed in Appendix B, we use a static LMOKE measurement to calibrate the Fe(8 nm) ZTS detector. To very good approximation, we infer  $b = (6.9 - 11.1i)$  m/V for the scaling factor in Eq. (3).

Subsequently, we use Eq. (2) to extract the incident THz electric field  $E_{\text{inc}}(t) = \mathbf{v} \cdot \mathbf{E}_{\text{inc}}(t)$  with  $\mathbf{v} \parallel \mathbf{E}_{\text{inc}}$  from the measured probe-ellipticity variation. The resulting  $E_{\text{inc}}(t)$  is in good agreement with the field extracted from EOS in the GaP detector, in terms of both shape and absolute amplitude (Fig. 3).

## V. ZTS APPLICATIONS

### A. THz field sampling

Our ZT THz detector Fe(8 nm) permits accurate sampling of intense THz fields (strength >0.1 MV/cm) over a bandwidth of 0.1–11 THz and beyond, without showing indications of saturation (see Fig. S2 [30]). This feature is crucial for virtually all nonlinear THz-spectroscopy experiments.

As a further proof of principle, we use our ZT detector for sampling of THz pulses generated through tilted-pulse-front excitation of LiNbO<sub>3</sub> (see Fig. S4 [30]). Again, the extracted THz electric field is in good agreement with the one obtained by EOS.

### B. EOS calibration

As a second application, we use our ZT detector to calibrate THz EO detectors. So far, the response function  $\tilde{H}(\omega)$  of EO detectors with zincblende structure, e.g., GaP and ZnTe, are calculated based on models with a number of parameters, such as a global scaling factor and the ratio of ionic versus electronic optical nonlinearity, the determination of which is not straightforward [19,39,40].

To determine  $\tilde{H}(\omega)$  of, for example, GaP(50  $\mu\text{m}$ ), we take the THz signals measured by ZTS in Fe(8 nm) and by EOS in GaP(50  $\mu\text{m}$ ), and make use of Eq. (2) and the fact that the THz excitation and optical probing conditions in the experiment are the same. We obtain the EO transfer function

$$\tilde{H}_{\text{GaP}}(\omega) = \frac{\tilde{S}_{\text{GaP}}(\omega)}{\tilde{S}_{\text{Fe}}(\omega)} \tilde{H}_{\text{Fe}}(\omega), \quad (6)$$

the frequency dependence of which directly follows from the measured signals  $S_{\text{GaP}}$  and  $S_{\text{Fe}}$  and Eq. (3).

Figure 4(a) shows the amplitude spectra of  $S_{\text{GaP}}$  and  $S_{\text{Fe}}$  and illustrates the low-pass behavior of ZTS [Eq. (3)]. The spectral amplitude and phase of  $\tilde{H}_{\text{GaP}}(\omega)$  resulting from Eq. (6) are displayed in Fig. 4(b). They agree well with model calculations [Fig. 4(c)]. For comparison, the calculated  $\tilde{H}_{\text{Fe}}(\omega)$  is shown in Fig. 4(c), too.

### C. ZTS modulation

A third outstanding functionality of the ZT detector follows from Eq. (2). The measured signal is proportional to the projection  $\mathbf{v} \cdot \mathbf{E}_{\text{inc}}$  of the incident THz electric field  $\mathbf{E}_{\text{inc}}$  on the magnetization direction  $\mathbf{v} = \mathbf{M}/|\mathbf{M}_0|$ . Therefore, we can easily modulate the sign of  $\tilde{H}_{\text{Fe}}(\omega)$  by periodically changing the magnetization of the ZT detector between  $-\mathbf{M}_0$  and  $+\mathbf{M}_0$ .

To demonstrate this THz demodulation scheme, we employ an ac electromagnet operating at a frequency of  $f_{\text{rep}}/2 = 500$  Hz, i.e., half the repetition rate of the THz pulses [38]. The delay time  $t$  is set to the maximum of the

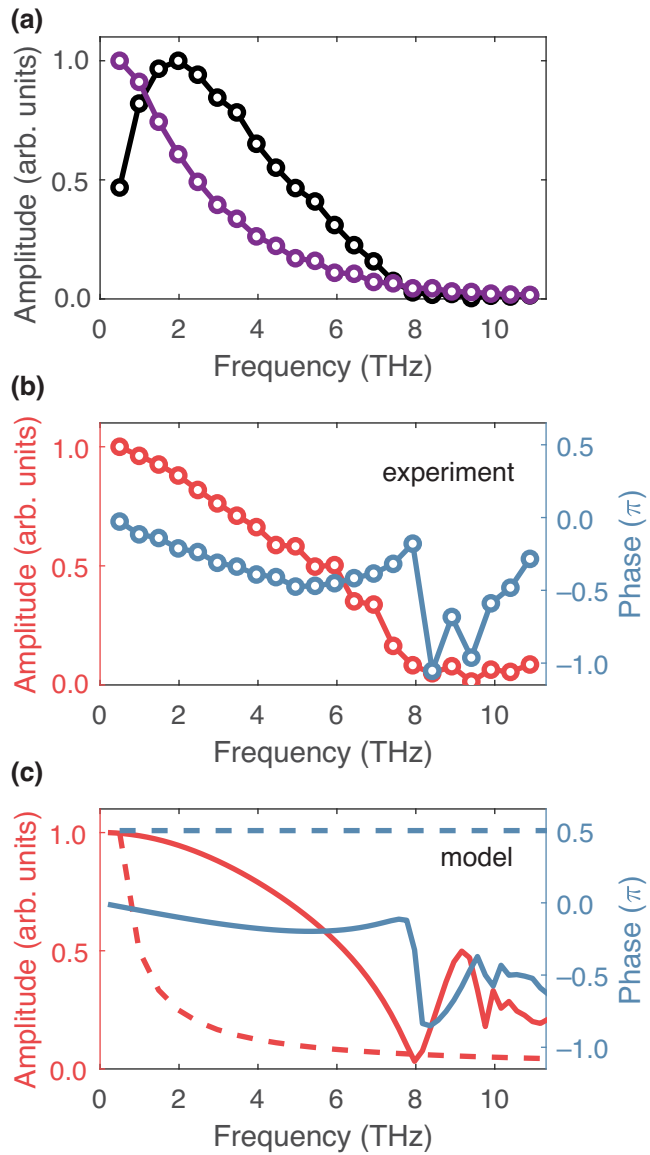


FIG. 4. EOS-response characterization by ZTS. (a) Fourier amplitude of the EOS signal from GaP(50  $\mu\text{m}$ ) (black) and the ZTS signal from Fe(8 nm) (purple). Prior to Fourier transformation, the signals are reduced to the echo-free time window from  $-1$  to  $+1$  ps [see Fig. 2(a)]. (b) Amplitude (red) and phase (blue) of the EOS transfer function  $\tilde{H}_{\text{GaP}}(\omega)$  for GaP(50  $\mu\text{m}$ ) obtained by referencing to the ZTS signal from Fe(8 nm). (c) Calculated response functions  $\tilde{H}_{\text{GaP}}(\omega)$  (solid curves) and  $\tilde{H}_{\text{Fe}}(\omega)$  (dashed curves).

ZT signal for one magnetization direction [Fig. 5(a)]. Thus, we modulate the Fe magnetization between  $\pm \mathbf{M}_0$  at  $f_{\text{rep}}/2$ , and signals are measured for each THz pulse at a rate of  $f_{\text{rep}}$ .

Figure 5(b) displays the signal recorded for some 50 subsequent pulses. The alternating signal amplitude clearly confirms the amplitude modulation of the ZT-detector

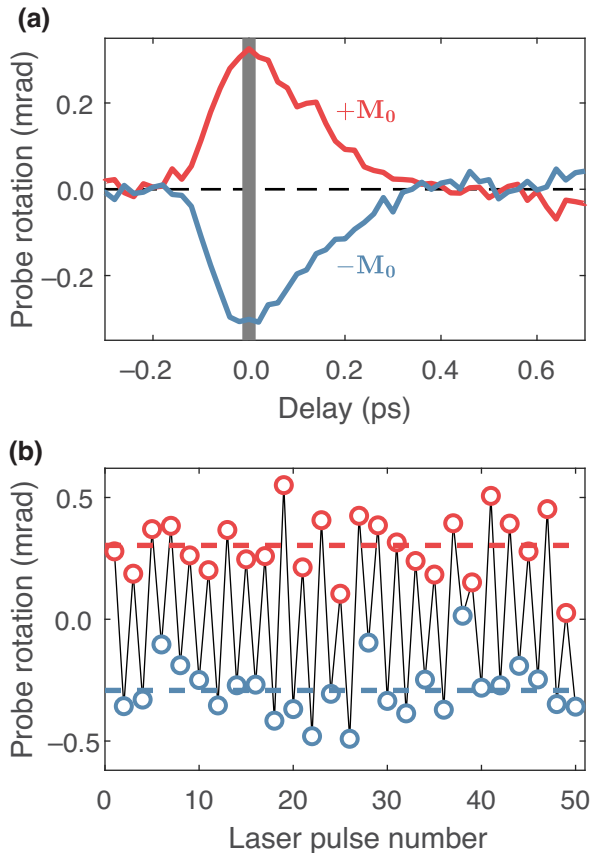


FIG. 5. Rapid amplitude modulation of the ZT detector. (a) ZTS signal of a BiIG sample for opposite magnetization directions  $\pm \mathbf{M}_0$ . (b) Pulse-to-pulse probe rotation when the garnet magnetization is modulated at half the laser repetition rate of  $f_{\text{rep}}/2 = 500$  Hz. The delay line is set to the maximum of the ZTS signal [see gray mark in panel (a)].

response at  $f_{\text{rep}}/2 = 500$  Hz. While this frequency is limited by the laser-pulse repetition rate, modulation frequencies of several 10 kHz, or even 1 MHz, are feasible by sufficiently fast magnets [41], strain waves [42], or current-driven spin-orbit torques [43].

## VI. CONCLUSIONS

We demonstrate the detection of transient THz electric fields by ZTS. The ZT detector has outstanding features that enable interesting applications, for example, sampling of intense THz pulses with a strength of  $>0.1$  MV/cm with a straightforward gapless transfer function and known absolute magnitude, characterization of the response function of EO detectors, and modulation of the polarization sensitivity in a noncontact fashion by an external magnetic field.

The last feature is interesting for demodulation of the modulated THz waves in, for instance, low-noise lock-in detection schemes or data transfer without analog-to-digital conversion. Finally, our study may serve as a guide

for future works that aim to increase the sensitivity of ZT detectors.

## ACKNOWLEDGMENTS

The authors acknowledge funding by the DFG collaborative research center SFB TRR 227 “Ultrafast spin dynamics” (project ID 328545488, projects A05, B02, and B05), the DFG priority program SPP2314 INTEREST (project ITISA), and financial support from the Horizon 2020 Framework Program of the European Commission under FET Open Grant No. 863155 (s-Nebula).

T.S.S. and T.K. are shareholders of TeraSpinTec GmbH, and T.S.S. is an employee of TeraSpinTec GmbH.

## APPENDIX A . DERIVATION OF ZTS RESPONSE FUNCTION FOR THIN METALLIC FILMS

The magnetic field  $\mathbf{B}$  of the THz pulse inside the magnetic film exerts Zeeman torque on the magnetization  $\mathbf{M}$ . We assume small magnetization deflections [ $\mathbf{M} \approx \mathbf{M}_0$  on the right-hand side of Eq. (1)] and consider only free uniform precession. In particular, we neglect effects such as perpendicular standing spin waves, attenuation, and nutation [28,44,45].

In the frequency domain, the resulting out-of-plane magnetization component is given by Eq. (1). Following Fourier transformation  $\Delta\tilde{\mathbf{M}}(\omega, z) = \int dt \Delta\mathbf{M}(t, z) e^{i\omega t}$ , Eq. (1) turns into

$$\Delta\tilde{\mathbf{M}}(\omega, z) = -\frac{\gamma}{i\omega} \mathbf{M}_0 \times \tilde{\mathbf{B}}(\omega, z). \quad (\text{A1})$$

Assuming the magnetic medium has cubic symmetry for  $\mathbf{M}_0 = 0$ , the transient out-of-plane magnetization gives rise to off-diagonal elements  $\Delta\tilde{\varepsilon}_{yx}(\omega, z) = -\Delta\tilde{\varepsilon}_{xy}(\omega, z)$  of the dielectric permittivity tensor, where  $\Delta\tilde{\varepsilon}_{yx}(\omega, z) = iQ\varepsilon_2 \mathbf{u}_z \cdot \Delta\tilde{\mathbf{M}}(\omega, z)/|\mathbf{M}_0|$ ,  $\mathbf{u}_z$  is the unit vector along the  $z$  axis,  $Q \propto |\mathbf{M}_0|$  is the Voigt magneto-optic coefficient, and  $\varepsilon_2$  is the dielectric permittivity of the metal film at the mean probe frequency. The tensor element  $\Delta\tilde{\varepsilon}_{yx}(\omega, z)$  results in magnetic circular birefringence (Faraday effect) and modulates the probe polarization.

To calculate the probe-polarization change, we consider  $\Delta\tilde{\varepsilon}_{yx}(\omega, z)$  as a small perturbation [46,47]. As the film is thin with respect to the THz and visible wavelengths, and because the probe resides within the film for a minor amount of time, we assume instantaneous sampling of the entire film by the probe. Likewise, we neglect the dependence of the optical coefficients on the probe frequency  $\omega_{\text{pr}}$  over the probe spectrum.

With the unperturbed probe field with amplitude  $\mathbf{E}_{\text{pr}0}(\omega_{\text{pr}}, z)$  linearly polarized along the  $x$  axis, we obtain

the first-order change  $\Delta\mathbf{E}_{\text{pr}}(\omega_{\text{pr}}, z)$  in the probe-field polarized along the  $y$  axis as [46]

$$\Delta\tilde{E}_{\text{pr}}(\omega_{\text{pr}}, z) = -\frac{\omega_{\text{pr}}^2}{c^2} \int_0^d dz' G_{z'}(\omega_{\text{pr}}, z) \Delta\tilde{\varepsilon}_{yx}(\omega, z') E_{\text{pr}0}(\omega_{\text{pr}}, z'). \quad (\text{A2})$$

Here,  $d$  is the thickness of the metal film, and  $G_{z'}(\omega_{\text{pr}}, z)$  is the known electric field Green function of the structure for  $\tilde{\varepsilon}_{yx} = 0$ . After substituting the corresponding expressions for  $G_{z'}(\omega_{\text{pr}}, z)$  and  $E_{\text{pr}0}(\omega_{\text{pr}}, z')$  [47], we obtain the complex-valued probe-polarization change behind the magnetic film ( $z = d$ ) according to

$$\tilde{S}(\omega) = \frac{\Delta\tilde{E}_{\text{pr}}(\omega_{\text{pr}}, d)}{\tilde{E}_{\text{pr}0}(\omega_{\text{pr}}, d)} = \frac{i\omega_{\text{pr}}^2}{2\beta_2 c^2} R(\omega_{\text{pr}}) \int_0^d dz \Delta\tilde{\varepsilon}_{yx}(\omega, z) \times (1 + r_{21}e^{2i\beta_2 z})(1 + r_{23}e^{2i\beta_2(d-z)}), \quad (\text{A3})$$

where  $\beta_2(\omega_{\text{pr}}) = n_2(\omega_{\text{pr}})\omega_{\text{pr}}/c$  is the angular spatial frequency of metal,  $r_{ij} = (n_i - n_j)/(n_i + n_j)$  are Fresnel reflection coefficients, and  $R = 1/(1 - r_{21}r_{23}e^{2i\beta_2 d})$  accounts for the multiple probe reflections in the metal film.

As shown in Fig. S5 [30], the last two factors of the integrand in Eq. (A3) can be approximated well by their values at  $z = d/2$  for the parameter values shown in Table S1 [30]. Considering Eq. (A1) and expressing  $\Delta\tilde{\varepsilon}_{yx}$  through the Voigt coefficient, we arrive at

$$\tilde{S}(\omega) = \frac{Q\beta_2}{2} \frac{(1 + r_{21}e^{i\beta_2 d})(1 + r_{23}e^{i\beta_2 d})}{1 - r_{21}r_{23}e^{2i\beta_2 d}} \times \frac{\gamma}{i\omega} \int_0^d dz \mathbf{u}_z \cdot [\mathbf{v} \times \tilde{\mathbf{B}}(\omega, z)], \quad (\text{A4})$$

with  $\mathbf{v} = \mathbf{M}_0/|\mathbf{M}_0|$ .

To determine  $\tilde{\mathbf{B}}(\omega, z)$ , we note that the studied Fe film has a thickness  $d$  much smaller than the THz wavelength and the THz attenuation length inside the film material. Therefore, the THz electric field is, to a very good approximation, constant across the film thickness. Its amplitude at frequency  $\omega$  is given by

$$\tilde{\mathbf{E}}(\omega) = \frac{2n_1(\omega)}{n_1(\omega) + n_3(\omega) + dZ_0\sigma(\omega)} \tilde{\mathbf{E}}_{\text{inc}}(\omega), \quad (\text{A5})$$

where  $\sigma(\omega)$  is the conductivity of the metal film, and  $Z_0$  is the vacuum impedance [38]. By using Eq. (A5) and Ampere's law, we obtain the magnetic field

$$\tilde{\mathbf{B}}(\omega, z) = \frac{2}{c} \frac{n_3(\omega) + (d - z)Z_0\sigma(\omega)}{n_1(\omega) + n_3(\omega) + dZ_0\sigma(\omega)} \mathbf{u}_z \times \tilde{\mathbf{E}}_{\text{inc}}(\omega), \quad (\text{A6})$$

and Eqs. (A4) and (A6) yield

$$\tilde{S}(\omega) = \frac{Q\beta_2 d}{2} \frac{(1 + r_{21}e^{i\beta_2 d})(1 + r_{23}e^{i\beta_2 d})}{1 - r_{21}r_{23}e^{2i\beta_2 d}} \times \frac{\gamma}{i\omega c} \frac{2n_3(\omega) + Z_0d\sigma(\omega)}{n_1(\omega) + n_3(\omega) + Z_0d\sigma(\omega)} \mathbf{v} \cdot \tilde{\mathbf{E}}_{\text{inc}}(\omega). \quad (\text{A7})$$

We note that the term in front of  $\mathbf{v} \cdot \tilde{\mathbf{E}}_{\text{inc}}$  in Eq. (A7) is constant over the whole bandwidth of 0.1–10 THz (see Fig. S6 [30]) and can be well approximated by its value at  $\omega = 0$  for the parameters listed in Table S1 [30].

As a consequence, the ZTS response finally becomes

$$\tilde{S}(\omega) = C_{\text{pr}}C_{\mathbf{E}}(\omega)\mathbf{v} \cdot \tilde{\mathbf{E}}_{\text{inc}}(\omega) \quad (\text{A8})$$

with

$$C_{\text{pr}} = -\frac{Q\beta_2 d}{2} \frac{(1 + r_{21}e^{i\beta_2 d})(1 + r_{23}e^{i\beta_2 d})}{1 - r_{21}r_{23}e^{2i\beta_2 d}},$$

$$C_{\mathbf{E}}(\omega) = -\frac{\gamma}{i\omega c} \frac{2n_3(\omega) + Z_0d\sigma_0}{n_1(\omega) + n_3(\omega) + Z_0d\sigma_0}. \quad (\text{A9})$$

Note that the prefactor  $-Q\beta_2 d/2$  is the complex-valued Faraday rotation for a thick magnetic film [34].

## APPENDIX B . ZEEMAN-DETECTOR CALIBRATION

As seen from Eqs. (A8) and (A9), the transfer function of a metal-film-based Zeeman detector is fully determined by its THz and optical refractive indices, THz conductivity, and magneto-optic Voigt parameter. In contrast to EOS crystals, all required values can be measured using linear optical and THz spectroscopies. Here, we limit ourselves to the experimental determination of the magneto-optic Voigt parameter  $Q$  while all other values are taken from the literature (see Table S1 [30]) [38,48–50].

In the experiment, we use a reflection geometry (angle of incidence 52°, *s*-polarized probe) and magnetize our Fe sample along the *x* axis [Fig. 1(b)], corresponding to the so-called LMOKE geometry. By measuring both rotation and ellipticity variations of the probe polarization, we obtain the complex-valued LMOKE signal  $S = 0.0016 - 0.0011i$  (see Fig. S7 [30]). As the magneto-optic Voigt parameter  $Q$  is small, the response is linear, i.e.,  $S = aQ$  with coefficient  $a$ . Using a 4 × 4-transfer-matrix formalism [51,52], we numerically determine the value of  $a$  for an Fe film on a glass substrate using the parameter values listed in Table S1 [30]. Finally, we obtain  $Q = S/a = 0.060 - 0.001i$ , calculate the ZTS transfer function  $\tilde{H}(\omega)$  [Eqs. (A8) and (A9)], and arrive at the results shown in Fig. 3. To very good approximation, we find  $\tilde{H}(\omega) = b/i\omega$ , consistent with Eq. (3), where  $b$  is  $(-6.1 + 11.1i)$  m/V for our Fe(8 nm) ZTS detector.

It is important to note that both  $Q$  and  $n_2(\omega_{\text{pr}})$  are reported to be thickness dependent in thin Fe films [49,53]. Here, we use an effective refractive-index value obtained for an Fe thin film with a thickness of 12 nm [49]. For even better results, it is advisable to determine the refractive index for the studied film separately. Additionally, one can use epitaxially grown films [53], where the impact of the thickness dependence is smaller compared to sputter-deposited samples [49].

- [1] K.-L. Yeh, M. C. Hoffmann, J. Hebling, B. Bartal, and K. A. Nelson, Generation of high-power terahertz pulses by tilted-pulse-front excitation and their application possibilities, *J. Opt. Soc. Am. B* **25**, B6 (2008).
- [2] M. Raeiszadeh, X. Ropagnol, M. A. Gauthier, A. Laramée, C. Y. Côté, M. Reid, M. Khorasaninejad, T. Ozaki, S. Safavi-Naeini, and M. Bouvier, Intense THz pulses with large ponderomotive potential generated from large aperture photoconductive antennas, *Opt. Express* **24**, 11299 (2016).
- [3] A. Nguyen, R. Bouillaud, L. Bergé, E. Cormier, B. Zhou, S. Skupin, P. U. Jepsen, K. J. Kaltenecker, I. Thiele, J.-C. Delagnes, N. Fedorov, and D. Descamps, Wavelength scaling of terahertz pulse energies delivered by two-color air plasmas, *Opt. Lett.* **44**, 1488 (2019).
- [4] J. András Fülöp, S. Tzortzakis, and T. Kampfrath, Laser-driven strong-field terahertz sources, *Adv. Opt. Mater.* **8**, 1900681 (2020).
- [5] C. Rader, Z. B. Zaccardi, S. H. E. Ho, K. G. Harrell, P. K. Petersen, M. F. Nielson, H. Stephan, N. K. Green, D. J. H. Ludlow, M. J. Lutz, S. J. Smith, D. J. Michaelis, and J. A. Johnson, A new standard in high-field terahertz generation: The organic nonlinear optical crystal PNPA, *ACS Photonics* **9**, 3720 (2022).
- [6] R. Rouzegar, A. L. Chekhov, Y. Behovits, B. R. Serrano, M. A. Syskaki, C. H. Lambert, D. Engel, U. Martens, M. Münzenberg, M. Wolf, G. Jakob, M. Kläui, T. S. Seifert, and T. Kampfrath, Broadband Spintronic Terahertz Source with Peak Electric Fields Exceeding 1.5 MV/cm, *Phys. Rev. Appl.* **19**, 034018 (2023).
- [7] T. Kampfrath, K. Tanaka, and K. A. Nelson, Resonant and nonresonant control over matter and light by intense terahertz transients, *Nat. Photonics* **7**, 680 (2013).
- [8] H. Y. Hwang, S. Fleischer, N. C. Brandt, B. G. Perkins, M. Liu, K. Fan, A. Sternbach, X. Zhang, R. D. Averitt, and K. A. Nelson, A review of non-linear terahertz spectroscopy with ultrashort tabletop-laser pulses, *J. Mod. Opt.* **62**, 1447 (2014).
- [9] D. Nicoletti and A. Cavalleri, Nonlinear light–matter interaction at terahertz frequencies, *Adv. Opt. Photonics* **8**, 401 (2016).
- [10] S. Baierl, J. H. Mentink, M. Hohenleutner, L. Braun, T. M. Do, C. Lange, A. Sell, M. Fiebig, G. Woltersdorf, T. Kampfrath, and R. Huber, Terahertz-Driven Nonlinear Spin Response of Antiferromagnetic Nickel Oxide, *Phys. Rev. Lett.* **117**, 197201 (2016).

- [11] J. Lu, X. Li, H. Y. Hwang, B. K. Ofori-Okai, T. Kurihara, T. Suemoto, and K. A. Nelson, Coherent Two-Dimensional Terahertz Magnetic Resonance Spectroscopy of Collective Spin Waves, *Phys. Rev. Lett.* **118**, 207204 (2017).
- [12] Y. Behovits, A. L. Chekhov, S. Y. Bodnar, O. Gueckstock, S. Reimers, T. S. Seifert, M. Wolf, O. Gomonay, M. Kläui, M. Jourdan, and T. Kampfrath, Terahertz Néel spin-orbit torques drive nonlinear magnon dynamics in antiferromagnetic Mn<sub>2</sub>Au, *Nat. Commun.* (2023) (to be published).
- [13] Z. Zhang, F. Sekiguchi, T. Moriyama, S. C. Furuya, M. Sato, T. Satoh, Y. Mukai, K. Tanaka, T. Yamamoto, H. Kageyama, Y. Kanemitsu, and H. Hirori, Generation of third-harmonic spin oscillation from strong spin precession induced by terahertz magnetic near fields, *Nat. Commun.* **14**, 1 (2023).
- [14] E. A. Mashkovich, K. A. Grishunin, R. M. Dubrovin, A. K. Zvezdin, R. V. Pisarev, and A. V. Kimel, Terahertz light-driven coupling of antiferromagnetic spins to lattice, *Science* **374**, 1608 (2021).
- [15] H. Elgabarty, T. Kampfrath, D. J. Bonthuis, V. Balos, N. K. Kaliannan, P. Loche, R. R. Netz, M. Wolf, T. D. Kühne, and M. Sajadi, Energy transfer within the hydrogen bonding network of water following resonant terahertz excitation, *Sci. Adv.* **6**, eaay7074 (2020).
- [16] A. Stupakiewicz, C. S. Davies, K. Szerenos, D. Afanasiev, K. S. Rabinovich, A. V. Boris, A. Caviglia, A. V. Kimel, and A. Kirilyuk, Ultrafast phononic switching of magnetization, *Nat. Phys.* **17**, 489 (2021).
- [17] D. Afanasiev, J. R. Hortensius, B. A. Ivanov, A. Sasani, E. Bousquet, Y. M. Blanter, R. V. Mikhaylovskiy, A. V. Kimel, and A. D. Caviglia, Ultrafast control of magnetic interactions via light-driven phonons, *Nat. Mater.* **20**, 607 (2021).
- [18] A. S. Disa, J. Curtis, M. Fechner, A. Liu, A. von Hoegen, M. Först, T. F. Nova, P. Narang, A. Maljuk, A. V. Boris, B. Keimer, and A. Cavalleri, Photo-induced high-temperature ferromagnetism in YTiO<sub>3</sub>, *Nature* **617**, 73 (2023).
- [19] A. Leitenstorfer, S. Hunsche, J. Shah, M. C. Nuss, and W. H. Knox, Detectors and sources for ultrabroadband electro-optic sampling: Experiment and theory, *Appl. Phys. Lett.* **74**, 1516 (1999).
- [20] H. Zhao, Y. Tan, T. Wu, G. Steinfeld, Y. Zhang, C. Zhang, L. Zhang, and M. Shalaby, Efficient broadband terahertz generation from organic crystal BNA using near infrared pump, *Appl. Phys. Lett.* **114**, 241101 (2019).
- [21] T. Seifert, *et al.*, Efficient metallic spintronic emitters of ultrabroadband terahertz radiation, *Nat. Photonics* **10**, 483 (2016).
- [22] C. Vicario, C. Ruchert, F. Ardana-Lamas, P. M. Derlet, B. Tudu, J. Luning, and C. P. Hauri, Off-resonant magnetization dynamics phase-locked to an intense phase-stable terahertz transient, *Nat. Photonics* **7**, 720 (2013).
- [23] Y. Mukai, H. Hirori, T. Yamamoto, H. Kageyama, and K. Tanaka, Nonlinear magnetization dynamics of antiferromagnetic spin resonance induced by intense terahertz magnetic field, *New J. Phys.* **18**, 013045 (2016).
- [24] S. Bonetti, M. C. Hoffmann, M. J. Sher, Z. Chen, S. H. Yang, M. G. Samant, S. S. P. Parkin, and H. A. Dürr, THz-Driven Ultrafast Spin-Lattice Scattering in Amorphous Metallic Ferromagnets, *Phys. Rev. Lett.* **117**, 087205 (2016).
- [25] M. Shalaby, A. Donges, K. Carva, R. Allenspach, P. M. Oppeneer, U. Nowak, and C. P. Hauri, Coherent and incoherent ultrafast magnetization dynamics in 3d ferromagnets driven by extreme terahertz fields, *Phys. Rev. B* **98**, 014405 (2018).
- [26] B. C. Choi, J. Rudge, K. Jordan, and T. Genet, Terahertz excitation of spin dynamics in ferromagnetic thin films incorporated in metallic spintronic-THz-emitter, *Appl. Phys. Lett.* **116**, 132406 (2020).
- [27] T. G. H. Blank, K. A. Grishunin, E. A. Mashkovich, M. V. Logunov, A. K. Zvezdin, and A. V. Kimel, THz-Scale Field-Induced Spin Dynamics in Ferrimagnetic Iron Garnets, *Phys. Rev. Lett.* **127**, 037203 (2021).
- [28] R. Salikhov, I. Ilyakov, L. Körber, A. Kákay, R. A. Gallardo, A. Ponomaryov, J. C. Deinert, T. V. A. G. de Oliveira, K. Lenz, J. Fassbender, S. Bonetti, O. Hellwig, J. Lindner, and S. Kovalev, Coupling of terahertz light with nanometre-wavelength magnon modes via spin-orbit torque, *Nat. Phys.* **19**, 529 (2023).
- [29] S. Sederberg, D. Zimin, S. Keiber, F. Siegrist, M. S. Wissmer, V. S. Yakovlev, I. Floss, C. Lemell, J. Burgdörfer, M. Schultze, F. Krausz, and N. Karpowicz, Attosecond optoelectronic field measurement in solids, *Nat. Commun.* **11**, 1 (2020).
- [30] See the Supplemental Material at <http://link.aps.org/supplemental/10.1103/PhysRevApplied.20.034037> for more figures, data and details.
- [31] S. F. Maehrlein, I. Radu, P. Maldonado, A. Paarmann, M. Gensch, A. M. Kalashnikova, R. V. Pisarev, M. Wolf, P. M. Oppeneer, J. Barker, and T. Kampfrath, Dissecting spin-phonon equilibration in ferrimagnetic insulators by ultrafast lattice excitation, *Sci. Adv.* **4**, eaar5164 (2018).
- [32] J. Faure, J. Van Tilborg, R. A. Kaindl, and W. P. Leemans, Modelling laser-based table-top THz sources: Optical rectification, propagation and electro-optic sampling, *Opt. Quantum Electron.* **36**, 681 (2004).
- [33] T. Kampfrath, J. Nötzold, and M. Wolf, Sampling of broadband terahertz pulses with thick electro-optic crystals, *Appl. Phys. Lett.* **90**, 231113 (2007).
- [34] A. K. Zvezdin and V. A. Kotov, *Modern Magneto optics and Magneto optical Materials* (Taylor & Francis Group, New York, 1997).
- [35] G. Neuber, R. Rauer, J. Kunze, T. Korn, C. Pels, G. Meier, U. Merkt, J. Bäckström, and M. Rübhausen, Temperature-dependent spectral generalized magneto-optical ellipsometry, *Appl. Phys. Lett.* **83**, 4509 (2003).
- [36] P. Novák, *4.1.5 Optical and Magnetooptical Properties Landolt-Börnstein - Group III Condensed Matter 27E (Garnets)* (Springer-Verlag, Berlin Heidelberg, 1991).
- [37] A. Frej, C. S. Davies, A. Kirilyuk, and A. Stupakiewicz, Laser-induced excitation and decay of coherent optical phonon modes in an iron garnet, *J. Magn. Magn. Mater.* **568**, 170416 (2023).
- [38] A. L. Chekhov, Y. Behovits, J. J. F. Heitz, C. Denker, D. A. Reiss, M. Wolf, M. Weinelt, P. W. Brouwer, M. Münzenberg, and T. Kampfrath, Ultrafast Demagnetization of Iron

- Induced by Optical versus Terahertz Pulses, [Phys. Rev. X \*\*11\*\*, 041055 \(2021\)](#).
- [39] Y. U. Berozashvili, S. Machavariani, A. Natsvlishvili, and A. Chirakadze, Dispersion of the linear electro-optic coefficients and the non-linear susceptibility in GaP, [J. Phys. D: Appl. Phys. \*\*22\*\*, 682 \(1989\)](#).
- [40] W. L. Faust and C. H. Henry, Mixing of Visible and Near-Resonance Infrared Light in GaP, [Phys. Rev. Lett. \*\*17\*\*, 1265 \(1966\)](#).
- [41] O. Gueckstock, O. Gueckstock, L. Nádvorník, L. Nádvorník, L. Nádvorník, T. S. Seifert, T. S. Seifert, M. Borchert, M. Borchert, G. Jakob, G. Schmidt, G. Woltersdorf, M. Kläui, M. Wolf, T. Kampfrath, and T. Kampfrath, Modulating the polarization of broadband terahertz pulses from a spintronic emitter at rates up to 10 kHz, [Optica \*\*8\*\*, 1013 \(2021\)](#).
- [42] G. Lezier, P. Koleják, J. F. Lampin, K. Postava, M. Vanwolleghem, and N. Tiercelin, Fully reversible magnetoelectric voltage controlled THz polarization rotation in magnetostrictive spintronic emitters on PMN-PT, [Appl. Phys. Lett. \*\*120\*\*, 152404 \(2022\)](#).
- [43] K. Garello, C. O. Avci, I. M. Miron, M. Baumgartner, A. Ghosh, S. Auffret, O. Boulle, G. Gaudin, and P. Gambardella, Ultrafast magnetization switching by spin-orbit torques, [Appl. Phys. Lett. \*\*105\*\*, 212402 \(2014\)](#).
- [44] L. Brandt, U. Ritzmann, N. Liebing, M. Ribow, I. Razdolski, P. Brouwer, A. Melnikov, and G. Woltersdorf, Effective exchange interaction for terahertz spin waves in iron layers, [Phys. Rev. B \*\*104\*\*, 094415 \(2021\)](#).
- [45] K. Neeraj, *et al.*, Inertial spin dynamics in ferromagnets, [Nat. Phys. \*\*17\*\*, 245 \(2020\)](#).
- [46] D. L. Mills, *Nonlinear Optics* (Springer Berlin Heidelberg, Berlin, Heidelberg, 1998).
- [47] T. Kampfrath, *Charge-Carrier Dynamics in Solids and Gases Observed by Time-Resolved Terahertz Spectroscopy* (Freie Universität Berlin, Berlin, 2006).
- [48] T. J. Parker, J. E. Ford, and W. G. Chambers, The optical constants of pure fused quartz in the far-infrared, [Infrared Phys. \*\*18\*\*, 215 \(1978\)](#).
- [49] O. Maximova, S. Lyaschenko, I. Tarasov, I. Yakovlev, Y. Mikhlin, S. Varnakov, and S. Ovchinnikov, The magneto-optical Voigt parameter from magneto-optical ellipsometry data for multilayer samples with single ferromagnetic layer, [Phys. Solid State \*\*63\*\*, 1485 \(2021\)](#).
- [50] I. H. Malitson, Interspecimen comparison of the refractive index of fused silica, [J. Opt. Soc. Am. B \*\*55\*\*, 1205 \(1965\)](#).
- [51] J. Zak, E. R. Moog, C. Liu, and S. D. Bader, Fundamental magneto-optics, [J. Appl. Phys. \*\*68\*\*, 4203 \(1990\)](#).
- [52] C. Y. You and S. C. Shin, Generalized analytic formulae for magneto-optical Kerr effects, [J. Appl. Phys. \*\*84\*\*, 541 \(1998\)](#).
- [53] M. Buchmeier, R. Schreiber, D. E. Bürgler, and C. M. Schneider, Thickness dependence of linear and quadratic magneto-optical Kerr effects in ultrathin Fe(001) films, [Phys. Rev. B \*\*79\*\*, 064402 \(2009\)](#).